Liquid exfoliated SnP_3 nanosheets for very high areal capacity lithium ion batteries

Ruiyuan Tian,[1+*] Aideen Griffin,[1+] Mark McCrystall,[1] Madeleine Breshears,[1] Andrew Harvey,[1] Cian Gabbett,[1] Dominik V. Horvath,[1] Claudia Backes,[2] Yu Ying,[3] Thomas Heine,[4,5,6] Sang-Hoon Park,[7] Joao Coelho,[7] Valeria Nicolosi,[7] Markus Nentwig,[8] Christopher Benndorf,[8] Oliver Oeckler,[8] Jonathan N. Coleman[1*]

[1]*School of Physics, CRANN & AMBER Research Centers, Trinity College Dublin, Dublin 2, Ireland*

[2]*Chair of Applied Physical Chemistry, University of Heidelberg, Im Neuenheimer Feld 253, 69120 Heidelberg, Germany*

[3]*Jiangsu Co-Innovation Centre of Efficient Processing and Utilization of Forest Resources, College of Chemical Engineering, Nanjing Forestry University, Nanjing 210037, China*

[4]*Chair of Theoretical Chemistry, Technische Universität Dresden, Bergstrasse 66,01069 Dresden, Germany*

[5]*Helmholtz-Zentrum Dresden-Rossendorf, Abteilung Ressourcenökologie, Forschungsstelle Leipzig, Permoserstr. 15, 04318 Leipzig, Germany*

[6]*Department of Chemistry, Yonsei University, 50 Yonsei-ro, Seodaemun-gu, Seoul 03722, Korea*

[7]*School of Chemistry, CRANN & AMBER Research Centers, Trinity College Dublin, Dublin 2, Ireland*

[8]*Institut für Mineralogie, Kristallographie und Materialwissenschaft, Scharnhorststr. 20, Universität Leipzig, Germany*

[*]colemaj@tcd.ie, rtian@tcd.ie

+These authors contributed equally

ABSTRACT: Increasing the energy density of lithium ion batteries requires the discovery of new electrode materials capable of achieving very high areal capacity. Here, liquid phase exfoliation was used to produce nanosheets of SnP_3, a 2D material with extremely high theoretical capacity of 1670 mAh g^{-1}. These nanosheets can be fabricated into solution-processed thin films for use as lithium storing anodes. To maximise their performance, carbon nanotubes have been incorporated into the electrodes to simultaneously enhance conductivity and toughness. As a result, electrodes of thickness >300 μm can be produced, which display active-mass-normalised capacities (~1657 mAh g^{-1}_{Active}) very close to the theoretical value. These materials show maximum specific (~1250 mAh $g^{-1}_{Electrode}$) and areal (>20 mAh cm^{-2}) capacities, which are at the state-of-the-art for 2D-based electrodes, coupled with good rate-performance and stability. In combination with commercial cathode materials, full-cells have been fabricated with areal capacities of ~29 mAh cm^{-2} and near-record energy densities approaching 1000 Wh L^{-1}.

The ongoing climate-change crisis has rendered research into energy generation and storage more important than ever. One very important goal within this field is to continuously improve the performance of lithium ion batteries. For example, increasing battery energy densities will accelerate the rollout of electric vehicles[1] and improve the potential for bulk energy storage.[2] Thus, battery electrode development is an important part of the technological component of climate stabilisation.

A significant component of battery research is the development of new electrode materials.[3] Among other things, such materials should have high specific lithium storage capacity combined with the potential to display high rate performance.[4] Ideally, they would also have the capability to store other ions beyond lithium, such as sodium or potassium.[5] Recently, much attention has focused on 2-dimensional layered materials for use in both anodes and cathodes.[6, 7] Such 2D materials consist of van der Waals bonded few-layer stacks of atomically thin sheets with the most well-known examples being graphene, boron nitride and MoS_2.[8] Such nanosheets can be produced by liquid exfoliation[9, 10] of layered materials or directly synthesised.[11] Layered 2D materials have both high surface areas and the ability to store large amounts of lithium (or Na, K, etc.) via intercalation between the layers or via conversion reactions.[6] Such materials are also expected to display high rate-performance due to the relatively high diffusivity of ions between the layers.[12, 13] Impressive specific capacity data (normalised to total electrode mass) has been reported for storage of lithium in electrodes based on graphene (700 mAh g^{-1})[14] and MoS_2 (1200 mAh g^{-1}),[15] while graphene/phosphorene composites have demonstrated sodium storage values of up to 1150 mAh g^{-1}.[16]

However, data on rate-performance for 2D-based electrodes has been mixed, with high nanosheet aspect ratios leading to low ionic diffusivity within electrolyte-filled pores, yielding rate-performance results which are often below expectations.[12] In addition, as practical batteries will require the maximisation of both areal capacity and energy density,[17] it must be possible to fabricate thick electrodes, which display stable cycling at specific capacities close to the theoretical value.[18] This has proven very challenging for 2D based electrodes. To our knowledge, only one paper[19] has described a 2D-based electrode with areal capacity above 4 mAh cm^{-2}. While that work described Nb_2C-based lithium-storing anodes with very high initial capacity of ~20 mAh cm^{-2}, the cycling stability was poor with the capacity falling by >65% over 50 cycles.

It is important to continue the search for previously unexplored 2D materials, which can resolve these problems, leading to high areal capacity with reasonable stability and decent rate

performance. One way to do this is to identify layered compounds consisting of elements known to react reversibility with lithium in a way that results in effective Li storage. For example, compounds containing group 14 and 15 elements such as Ge, Sn and P would be expected to yield high-capacity conversion-type anodes.[20] A vast number of layered materials is known to inorganic chemistry,[21] many of which can be exfoliated.[22] The chemical stability of late group-14 phosphides such as GeP_3 (ref[23]) and SnP_3 (ref[24]) has been demonstrated recently on grounds of first-principles calculations. Indeed, SnP_3 is a layered material with a theoretical storage capacity of 1670 mAh $g^{-1}$for both lithium and sodium. However, although SnP_3 has been tested as an anode material in its layered form, it has not quite lived up to its potential, displaying stable capacities of ~1000 mAh g^{-1} for lithium[25] and ~800 mAh g^{-1} for sodium,[26] somewhat below the theoretical values.

However, for any active material, achieving maximal performance is never guaranteed and depends heavily on the electrode architecture with particle morphology and binder/additive combination key factors. A number of studies have shown that liquid-processed, exfoliated nanosheets yield electrodes with much better capacity and stability than those fabricated from unexfoliated layered particles.[27] In addition, it has been shown that replacing the conductive additive and binder with a network of carbon nanotubes can maximise charge storage capacity for electrodes fabricated from both 2D [28-30] and non-2D [18] based electrodes. In addition, the presence of nanotubes toughens the electrode dramatically, increasing the achievable film thickness, and significantly increases the conductivity,[31] laying the foundations for good rate performance.[4, 32, 33] This implies that the combination of exfoliation of SnP_3 layered crystals to give nanosheets and the addition of carbon nanotubes might not only allow SnP_3-based electrodes to reach their theoretical capacity but also to demonstrate high areal capacity and so energy density. Here we demonstrate the production of SnP_3 nanosheets by liquid phase exfoliation (LPE) and their fabrication into nanotube-enhanced composite anodes. These anodes display the theoretical specific capacity associated with SnP_3 at thicknesses beyond 300 μm resulting in record areal capacities. We demonstrate that full-cells based on these electrodes display near-state-of-the-art energy and power densities.

RESULTS

Liquid exfoliation of SnP_3

Bulk material of SnP_3 was synthesised by mixing red phosphorous and tin with a small excess of P and heating under vacuum (see methods). After a number of annealing steps, we obtained a black polycrystalline substance which powder XRD analysis (Figure 1A, and Supplementary Figure 1 and Table 1) showed to be 97% SnP_3 with 3% Sn_3P_4 as a minority phase. Such bulk samples can be converted into nanosheets (see figure 1B for structure) using liquid phase exfoliation[9, 30, 34-36] by sonicating the powder in N-methyl-pyrrolidone (NMP) before removing unexfoliated material by centrifugation. The resulting sample was a black liquid with a solids content of 1-3 g L^{-1} (Figure 1B). Optical spectroscopy on such dispersions (Figure 1C) showed the extinction coefficient (ε) spectrum to be flat and featureless. Measurements using an integrating sphere[37] showed the extinction to be dominated by scattering (σ) with an absorption coefficient (α) which is relatively flat over the entire visible-NIR range with no band edge observed for photon energies above 0.825 eV (see Supplementary Figure 2 and 3 for more spectral information). TEM measurements showed the dispersion to contain only 2D nanosheets (Figure 1D) with no non-planar material observed. These nanosheets are relatively large with lateral sizes in the range 200-2000 nm (Figure 1E). In order to confirm the composition of the nanosheets, we performed energy dispersive X-ray spectroscopy (EDX) in the TEM, obtaining individual spectra for 36 different nanosheets. An example of such a spectrum is shown in Figure 1F and clearly shows peaks from O, P and Sn. To minimise error associated with individual EDX spectra, we assess the sample composition by plotting the P/Sn ratio of atomic populations, measured on individual nanosheets as a histogram in Figure 1G. This histogram has a clear peak at P/Sn=3 confirming the nanosheet stoichiometry to be as expected. Similarly, we plotted the ratio of O atoms to SnP_3 formula units as a histogram in Figure 1G inset. This graph shows relatively low levels of oxidation, typically < 5 O atoms per 100 formula units and implies the exfoliation process to be relatively non-destructive. SEM imaging of thin (< 1 μm) vacuum filtered films confirmed the samples to consist of only 2D nanosheets (Figure 1H). We can further investigate the structural integrity of the nanosheets by performing Raman spectroscopy on a vacuum-filtered film prepared from a liquid exfoliated dispersion. Such a spectrum is shown in Figure 1I and is very similar to a reference spectrum measured on the layered powder indicating that exfoliation has not induced changes to the structure. In addition, the mode positions agree reasonably well with theoretical predictions (see Supplementary Figure 4).

Size-selection of SnP_3

As typical samples prepared by liquid phase exfoliation tend to have broad size distributions, it is common to apply size-selection techniques. In addition, narrowing the size distribution facilitates more accurate thickness measurements by AFM.[35] Here we applied liquid cascade centrifugation[36] to generate five fractions (referred to as XL, L, M, S, XS in order of decreasing size), each prepared by removing large and small nanosheets in two centrifugation steps at different relative centrifugal forces (RCF, expressed in units of *g*, see methods). Example AFM and TEM images of nanosheets from the XL, M and S fractions are shown in Figure 2 A-C (see Supplementary Figures 5-6). Statistical measurements of nanosheet size and thickness were made for each fraction using both AFM and TEM. Nanosheet length and thickness (expressed as number of layers) distributions are plotted in Figure 2 D-E for the XL and S fractions. While size selection has clearly been achieved, the distributions are still relatively broad. Note that although the thickest nanosheets observed are hundreds of layers thick, the thinnest observed nanosheet was a bilayer, suggesting that thin nanosheets can be obtained if required. The mean nanosheet length and thickness per fraction are plotted versus the mean (or central) RCF used during size selection in Figure 2 F-G. In both cases the mean values scale roughly as $(RCF)^{-1/2}$ in line with previous reports.[36]

Recently, we showed that information about the intrinsic nanosheet mechanics can be extracted from data on the dimensions of LPE nanosheets.[35] Figure 2H shows nanosheet area plotted versus thickness on a flake-by-flake basis as measured by AFM. Such plots should be roughly quadratic[35] with extrapolation of the fit line to N = 1 giving the characteristic monolayer area. The square root of the monolayer area is the characteristic monolayer lateral size, D_{ML}, which has been shown to be directly related to the ratio of in-plane to out-of-plane Young's modulus of the nanosheet:

$$D_{ML} \approx 2h_0 \frac{Y_{In-plane}}{Y_{Out-of-plane}} \quad (1)$$

where h_0 = 0.35 nm is the SnP_3 monolayer thickness.[38] The data in figure 2H implies a value of D_{ML} = 8 nm yielding a modulus ratio of $Y_{In-plane} / Y_{Out-of-plane} \approx 10$, reasonably close to the values of 4-7 calculated for MoS_2, $MoSe_2$, WS_2 and WSe_2, but considerably smaller than values of ~30 found for materials such as BN and graphene.[35]

The AFM data in Figure 2H can be converted to nanosheet aspect ratio, which is plotted in the form of histograms in Figure 2I. The aspect ratio is largely independent of nanosheet size and tends to fall in the range 10-30 in all cases. These nanosheet aspect ratios are relatively low

compared to those found in graphene. However, such low aspect ratios are probably desirable in battery electrodes because of the link between high-aspect ratios and long diffusion times.[12]

Storage of lithium using SnP_3

As described in the introduction, liquid exfoliated SnP_3 is a very promising lithium storing material with high theoretical capacitance of 1670 mAh g^{-1}. In addition, as we have shown in Figure 2I, the nanosheet aspect ratio is relatively low, suggesting good rate-performance might be possible.[12] However, it remains a great challenge to maximise its energy storage performance. In general, the simplest way to maximise the energy density of full cells is to use thick electrodes with very high areal capacity. Once the electrodes are thick enough, the contribution of inactive material becomes negligible, leading to a cell energy density that is determined by the energy densities of the electrode materials.[18] The electrode areal capacity, Q/A, is related to specific capacity, Q/M_T, (or volumetric capacity, Q/V_T) and electrode loading, M_T/A (or thickness, L_E) via

$$\frac{Q}{A} = \frac{Q}{M_T}\frac{M_T}{A} = \frac{Q}{V_T}L_E \qquad (2)$$

where, M_T represents the total electrode mass. To maximise Q/A, it is first necessary to achieve maximal Q/M_T for electrodes with loading (or thickness) which is as large as possible. We can relate Q/M_T to the specific capacity normalised to active mass, Q/M_{Act} via

$$\frac{Q}{M_T} = \frac{Q}{M_{Act}} f_{Act} \qquad (3)$$

where f_{Act} is the mass fraction of active material. Thus, to maximise Q/A it is necessary to achieve the theoretical maximum value of Q/M_{Act} while maximising f_{Act}. A number of studies have shown that Q/M_{Act} can be maximised by using optimised conductive additives to maximise electrode conductively allowing efficient charge delivery to all parts of the electrode.[29, 39]

The second requirement is to achieve this for very thick electrodes. Producing thick electrodes from liquid dispersions is challenging because mechanical instabilities during drying lead to a maximum achievable thickness, the critical crack thickness (CCT), which tends to be ~100 um for traditional electrode formulations.[18] It is known that the CCT can be increased significantly by improving the mechanical properties of the electrode material.[18]

We have previously shown that both of these requirements can be achieved simultaneously by using carbon nanotubes as a combination of mechanical binder and conductive additive.[18]

Nanotube networks within battery electrodes have been shown to yield much higher conductivities compared to traditional additives such as carbon black or even state of the art additives such as graphene.[32] In addition, the high toughness of such networks dramatically enhances the CCT, allowing the formulation of electrodes as thick as 800 μm.[18] The enhanced conductivity will reduce the degradation of rate performance at high electrode thickness,[32, 33] while the increased mechanical robustness supresses cracking during cycling, contributing to the stability of the electrode. Overall, nanotube enabled electrodes have shown very promising performance.[29, 40]

We prepared composite dispersions by mixing standard sample dispersions of liquid exfoliated SnP_3 nanosheets with dispersions of single-walled carbon nanotubes without any additional binder. In this way, the mass fraction of nanotubes, M_f, can easily be tuned ($M_f = M_{NT} / (M_{NT} + M_{Act}) = 1 - f_{Act}$). Using vacuum filtration, these composite dispersions were fabricated into films with typical thicknesses > 8 μm (0.4 mg cm^{-2}). Such films had a mean density of ~1.3 g cm^{-3} and mean porosities of ~60% which should accommodate some degree of volume change associated with charging (see Supplementary Figure 7). Figure 3A shows an SEM image of a cross section of such a film (M_f = 25%, M_T/A = 2.3 mg cm^{-2}). These films are relatively uniform (figure 3A-B), with nanotubes distributed throughout the electrode and well interconnected with all SnP_3 particles. While SnP_3 nanosheets are observed within these electrodes, most of the SnP_3 is found as thicker particles (up to 300-400 nm thick). This contrasts with the relatively thin exfoliated nanosheets observed both in dispersion (figure 2) and in thin films (figure 1H). This implies a considerable degree of nanosheet re-aggregation during the formation of these thick films.

We investigated the electrochemical response of the SnP_3/CNT electrodes using cyclic voltammetry (CV, figure 3C). We see relatively narrow reduction peaks at 0.2, 0.5 and 0.8 V and oxidation peaks at 0.6, 0.8 and 1.3 V. These peaks are very similar to those observed previously for unexfoliated SnP_3.[25] Combining CV with EXAFS, Park et al.[25] showed this set of redox peaks to be consistent with a reversible combination of an intercalation reaction and a conversion reaction. For example, during discharge these reactions are:

$$SnP_3 + xLi \rightarrow Li_xSnP_3 (x \leq 4) \qquad \text{(intercalation)}$$

followed by

$$Li_xSnP_3 (x \leq 4) + (13.25\text{-}x)Li \rightarrow Li_{4.25}Sn + 3Li_3P \qquad \text{(conversion)}$$

implying that 13.25 charges can be stored per formula unit of SnP_3, equivalent to a capacity of 1670 mAh g^{-1}. We note that, even though this reaction is reversible, the repeated conversion and recombination of the material, coupled with the associated volume changes, result in significant changes in electrode morphology (Figure 3C inset). As shown in Supplementary Figure 8, the electrode thickness almost doubles over the course of 50 cycles. That such a change does not significantly degrade the capacity indicates that the nanotube network retains good electrical and mechanical integrity even in the face of significant morphological change.

We quantified the lithium storage capacity of this material by performing galvanostatic charge-discharge (GCD) measurements on SnP_3/CNT electrodes with various CNT mass fractions (figure 3D). These curves are similar to those previously[25] observed for unexfoliated SnP_3 and show a general increase in capacity with increasing CNT content. The low-rate charging capacity, normalised to both total and active masses, is plotted in figure 3E as a function of nanotube mass fraction. We find that Q/M_{Act} increases with increasing M_f before saturating at ~1660 mAh g^{-1}, virtually identical to the theoretical capacity, once M_f exceeded 25%. This is an important result and confirms[18] that using nanotube networks as a combination of binder and conductive additive allows SnP_3 to reach its theoretical capacity. In contrast, Q/M_T increases initially, peaks at $M_f \approx 25\%$ before falling off as the nanotube component begins to dominate the sample. This shows that the optimised electrode will contain ~25% nanotubes and deliver a very high usable capacity of $Q/M_T \approx 1250$ mAh g^{-1}.

Having comprehensively surveyed the 2D battery literature,[12] we are confident that both of these Q/M_{Act} and Q/M_T values are very close to the state-of-the-art for 2D materials. The only paper we know of reporting a higher Q/M_{Act} was from Sun et al.[16] reporting $Q/M_{Act} = 2500$ mAh g^{-1} for graphene/phosphorene Na-storing electrodes with the nearest competitor being an MoS_2/graphene Li-storing electrode displaying $Q/M_{Act} = 1500$ mAh g^{-1}.[11] In terms of Q/M_T, we believe the previous 2D state-of-the-art was for Li-storing MoS_2 electrodes displaying Q/M_T values of 1250 mAh g^{-1}[29] and 1200 mAh g^{-1},[15] very similar to our value. We note that SnP_3 has the same theoretical capacity for sodium storage as it does for lithium,[26] implying that such record capacities might also be achievable for sodium (or even potassium) ion batteries.

We tested the rate performance of electrodes with various CNT contents as shown in figure 3F. We found the rate performance to increase with CNT content, saturating above $M_f \approx 20\%$ as charge transport within the electrode ceases to be rate limiting.[33] As a result, $M_f = 25\%$ yields

both optimised capacity and a maximisation of rate performance (with respect to nanotube content).

High areal capacity electrodes

Maximising the areal capacity of electrodes requires films which display capacities close to their theoretical values even at very high thickness. We have previously shown that this can be achieved by using nanotube networks to replace both binder and conductive additive.[18] To this end, we fabricated electrodes from standard sample SnP_3 nanosheets mixed with ~25% SWNT. The total mass loading (M_T/A) of the electrodes was varied from 3.4 mg cm^{-2} (thickness 8 μm) to 43.2 mg cm^{-2} (314 μm). Note that without adding nanotubes it is virtually imposible to produce robust nanosheet films of such high thicknesses.[31] We performed GCD measurements (figure 4A), obtaining the areal capacities Q/A as a function of M_T/A in each case. As shown in figure 4B, we find a linear increase in areal capacity with loading, exceeding 40 mAh cm^{-2} for the thickest electrodes. This is an extremely high areal capacity, competitive with the highest values ever observed (~45 mAh $cm^{-2}$for silicon/nanotube composites).[18] We note that the slope of the linear fit in figure 4B yields the specific capacity of the overall electrode (Q/M_T). Here we obtain a value of 1250 mAh g^{-1}, similar to the maximum value obtained from figure 3E and equivalent to the theoretical specific capacity (accounting for M_f = 25wt%) even at very high mass loadings.

In addition, the electrodes showed good cycling performance. The Coulomb efficiency was typically ~80% on the first cycle but approached 100% by the 4^{th} cycle (Supplementary Figure 9). The electrodes with mass loading up to 9.2 mAh cm^{-2} are reasonably stable (17% loss in charging capacity over 40 cycles) with the 17.3 mAh cm^{-2} electrode slightly less so (30% loss over 40 cycles) and higher loading electrodes somewhat more unstable (figure 4C). We note that such stability can only be achieved using SnP_3 nanosheets combined with SWNT. As shown in Supplementary Figure 10, electrodes fabricated with bulk SnP_3 and SWNT or bulk SnP_3 and traditional binder/additive formulations displayed extremely poor cycling stability.

To put this data in context, we note that the 17.3 mAh cm^{-2} sample displayed 14 mAh cm^{-2} after 40 cycles. Previously, in terms of areal capacity, the best performing 2D-based electrode was an Nb_2C-based system which displayed 7.5 mAh cm^{-2} after 40 cycles. We believe that our SnP_3/CNT system is the highest areal capacity 2D lithium-storing electrode yet reported.

We performed impedance spectroscopy on electrodes with three mass loadings as shown in figure 4D. Fitting (see Supplementary Figure 11 and Supplementary Table 3 for equivalent circuit and fit parameters) showed the charge transfer resistance to fall inversely with electrode

thickness, reaching 10 Ω for the thickest electrode. We attribute the fall-off with thickness to the fact that the total active nanosheet surface area increases with electrode thickness.[41] The charge transfer resistance is related to the exchange current density, j_0, via $R_{CT} = RT / n_e F j_0 A_{Act}$, where n_e = 1 is the number of electrons associated with the redox reaction, and A_{Act} is the active surface area. If the redox reactions occur at the nanosheet edge, then it can be shown (see Supplementary methods) that

$$R_{CT} = \frac{RT\langle L \rangle}{4 n_e F j_0 (1-P) A_0 L_E} \quad (4)$$

where $\langle L \rangle$ is the mean nanosheet length, P and A_0 are the electrode porosity and geometric area. Fitting this equation to the data (taking n_e = 1, $\langle L \rangle$ = 740 nm, P = 60% and A_0 = 1.13 cm^2) yields a value of j_0 = 1.6×10^{-3} mA cm^{-2} of nanosheet edge area. This converts to 0.1 e^{-1} s^{-1}nm^{-2} suggesting that the time associated with each charge transfer event is relatively short and so not rate limiting.[41]

The rate performance of these electrodes is also good, despite their significant thicknesses (figure 4F). Plotting areal capacity versus areal current (rather than specific capacity varies specific current) presents a true picture of absolute achievable capacities whereas plotting specific values of capacity and current can make thin film data look impressive in a way that is not achievable at high thickness. For all mass loadings we see the usual low-current plateau followed by a fall off at higher current. However, for the thickest sample (M_T/A = 17.3 mg cm^{-2}), we find an areal capacity of 7.1 mAh cm^{-2} measured at a current density of 14 mA cm^{-2}, implying a charging time of 30 mins. This compares very favourably with data for high-performance Si/Gr electrodes for example, which displayed ~6.5 mAh cm^{-2} measured at a current density of 0.64 mA cm^{-2} (10 h charging time).[42]

We have recently shown that rate data can be quantitatively analysed by plotting the measured capacity (here Q/A) versus the rate, R, defined as $R = (I / A) / (Q / A)$.[4, 32, 33] Such data can be fitted using a semi-empirical equation for fitting capacity-rate data which outputs three fit parameters to assess rate-performance:

$$\frac{Q}{A} = Q_A \left[1 - (R\tau)^n \left(1 - e^{-(R\tau)^{-n}} \right) \right] \quad (5)$$

Here Q_A is the specific capacity at very low rate while n is an exponent describing how rapidly Q/A decays at high rate with diffusion-limited electrodes showing n close to 0.5 while capacitive-limited (i.e. electrically limited) electrodes yield n roughly equal to 1. Most

importantly, τ is the characteristic time associated with charge/discharge. This parameter is particularly important as it is a measure of the characteristic rate above which *Q/A* starts to fall off. As such, τ is a metric for rate performance where low time constants mean fast charge/discharge and indicate good rate-performance.

We plot *Q/A* vs. *R* in Figure 4G for electrodes with a number of mass loadings with the corresponding fits to equation 2 shown as dashed lines. We find Q_A to scale linearly with thickness while *n* is constant at ~0.75 (see Supplementary Figure 12 for all fit parameters). More importantly, the τ-values increase with mass loading from 152 s for the thinnest electrode to 2772 s for the thickest. These values are rough measures of the minimum charge/discharge time where near-maximal capacity can be attained, so low values of τ represent fast rate performance. The dependence of τ on thickness has been well-documented and is predominately due to charge transport and diffusion effects within the electrode.[33, 43] We note that because both τ and Q_A both increase with increasing thickness, there is always a tradeoff between maximising capacity and rate performance.[4]

We can put the rate-performance of these materials in context by calculating L_E^2 / τ, where L_E is the electrode thickness. This parameter acts as a figure of merit for rate performance with large values of L_E^2 / τ desired.[12, 32, 33] We plot L_E^2 / τ vs. electrode thickness in Figure 4H for these SnP_3/SWNT electrodes with literature data for 2D-based battery electrodes shown for comparison (extracted from ref [12]). In general, at each thickness, we find L_E^2 / τ to be competitive with the best-performing 2D electrodes. However, most importantly, for thick electrodes which are of the most practical importance, L_E^2 / τ is among the highest of any 2D material. This is an important result as it shows our thick, high capacity electrodes to have superlative rate performance. We believe this is due to the nanosheet aggregation described above which further reduces the (already small) active particle aspect ratio, resulting in lower tortuosity and so faster liquid-phase ion diffusion.[12]

We have argued previously that the capacity-rate trade-off is optimised when τ / Q_A is minimised.[4] In most electrodes, this parameter will never be lower than ~0.01 cm^2/mA but can be > 1 cm^2/mA in poorly performing electrodes.[4] We find that our thickest anodes have $\tau / Q_A \approx 0.03$ cm^2/mA, close to the minimum value, confirming that these materials give near optimised combinations of capacity and rate performance.

Full cells

In order to fully demonstrate the promise of SnP_3 for battery applications, we fabricated full cells using anodes consisting of SnP_3 with 25wt% SWNT and cathodes fabricated from lithium nickel cobalt aluminium oxide (NCA) mixed with 0.5wt% SWNT. We tuned the masses of anode and cathode so that both would have the same areal capacity. Cells were fabricated with various combined total (i.e. including CNT) anode and cathode masses (M_{A+C}/A) from 18-225 mg cm^{-2} (see Supplementary Figure 13) Low-rate, galvanostatic charge discharge curves are shown in Figure 5A and show a significant increase in cell areal capacity, $(Q/A)_{Cell}$ with M_{A+C}/A. This increase is linear with a slope of 120 mAh g^{-1} (figure 5B). Those cells with $(Q/A)_{Cell} \leq 10$ mAh cm^{-2} (i.e. $M_{A+C}/A < 80$ mg cm^{-2}) are quite stable (Figure 5C) with Coulombic efficiency approaching 100% after 4 cycles (Supplementary Figure 14), although higher mass loading cells do display a non-trivial capacity fade. Rate performance for three mass loadings is shown in Figure 5D. The 81 mg cm^{-2} cell (the highest loading which displayed good stability) shows excellent rate performance, which exceeds most conventional cells and is competitive with ultra-high performance Si-based segregated network cells.[18]

Extremely high areal capacities lead to high energy densities.[18] Figure 5E shows data for the cell volumetric energy density, $(E/V)_{Cell}$, for our cells plotted against $(Q/A)_{Cell}$, with data for some other high-performance cells for comparison (see also Supplementary Figure 15).[18, 44] Here, $(E/V)_{Cell}$ includes contributions from separator and current collectors as well as active material. The 81 mg cm^{-2} which displays $(Q/A)_{Cell} \approx 10$ mAh cm^{-2} yields an energy density of ~825 Wh L^{-1}, surpassing the high performance graphite/NMC cells and reasonably close to the very high performance Si/NMC cells recently reported by us.[18] Modifying the derivation described in ref [18] yields an equation for the $(E/V)_{Cell}$ as a function of $(Q/A)_{Cell}$:

$$(E/V)_{Cell} = \left[\frac{1/V}{(Q/V)_A} + \frac{1/V}{(Q/V)_C} + \frac{t_{Inactive}/V}{(Q/A)_{Cell}} \right]^{-1} \quad (6)$$

where V is the cell operating voltage, $t_{Inactive}$ is the combined thickness of current collectors and separator, while $(Q/V)_A$ and $(Q/V)_C$ are the volumetric capacities of the anode and cathode. Fitting this equation to the data shows the most stable stable SnP_3-based cells ($(Q/A)_{Cell} \approx 10$ mAh cm^{-2}, 81 mg cm^{-2}) to display ~75% of the maximum possible energy density associated with infinitely high areal capacity. Shown in Figure 5F is a Ragone plot comparing cell areal energy versus areal power for the cell types shown in Figure 4E. This shows our highest loading

cells to compare very favourable to these high-performance cells in terms of both energy and power.

DISCUSSION

We have demonstrated that SnP_3 nanosheets can be produced by liquid phase exfoliation. These nanosheets have been mixed with carbon nanotubes to form high performance lithium storage anodes. For nanotube contents of ~25wt%, these anodes display the theoretical capacity expected for SnP_3 (when normalised to active mass) and record capacity for a 2D-based anode (when normalised to total electrode mass). The presence of the nanotubes allows the fabrication of electrodes with thickness exceeding 300 μm leading to the highest reported (stable) areal capacity for a 2D-based electrode. As a result, when combined with conventional cathode materials, we can achieve full cells with high cell capacity and near state-of-the-art energy density. Because SnP_3 has the same theoretical capacity for Na storage as it does for Li, we are confident that these results might be translated to producing very high-performance sodium ion batteries. Although the synthesis of SnP_3 on the laboratory scale is tedious, the process may be upscaled at a pilot plant level. This would most likely involve large-scale ball milling combined with automated pelletising. In addition, the liquid exfoliation process can almost certainly be upscaled via processes such as wet-jet milling.[45] Thus, we believe this material may be a candidate for use in practical batteries.

METHODS

Synthesis

Starting materials for the preparation of SnP_3 were powdered red phosphorus (98.9%, ABCR, Karlsruhe, Germany) and tin (99.999%, Fémipari Kútató Intézet, Budapest, Hungary). Prior to use, phosphorus was treated with boiling aqueous NaOH solution (w ≈ 25%) and washed several times with demineralized water and acetone. The powder was dried under vacuum and stored under dry argon atmosphere. The tin rod was cleaned with concentrated hydrochloric acid, demineralized water and acetone. The elements then were mixed in the atomic ratio of Sn:P = 0.3:1 and a total mass of 500 mg, and sealed in a silica glass ampule under argon atmosphere (dried over P_4O_{10}, silica gel and titanium sponge at 873 K). The sample was heated slowly to 673 K for 7 d and cooled to room temperature by switching off the furnace. Afterwards, the substance was ground to a fine powder and cold-pressed into a pellet of 6 mm diameter, placed into a small corundum crucible and again sealed in a silica ampule under

argon. The sample was then annealed at 673 K for 7 d. This procedure was repeated (heating for 11 d) after intermediate grinding and pelletising steps. The product is a black powder. Its purity was checked by powder X-ray diffraction (see Fig. S1 and Tab. S1), the sample contains ~3 wt% Sn_3P_4. SEM-EDX investigations were in good agreement (Sn : P = 26(1) : 74 (1) at%, eight points) with the expected composition SnP_3.

Exfoliation

The powder was sonicated (tapered tip, VibraCell CVX, 750W) in 30 mL of 1-methyl-2-pyrridone (NMP, Sigma Aldrich HLPC grade ≥ 99%) for 5 h at pulse of 6 s on and 2 s off and an amplitude of 25%. The dispersion was then centrifuged in a Hettich Mikro 220R centrifuge equipped with a fixed-angle rotor 1016 at 26 *g* and the supernatant retained. The sediment was redispersed in 30 mL fresh NMP and exfoliated again for 16 h (overnight). The dispersion was centrifuged at 26 *g* and supernatant retained. The exfoliation procedure above was then repeated such that 4 × 26 *g* supernatant samples were produced. These samples were centrifuged at 2.6 k *g* and the sediment of each was redispersed in 5 mL IPA to give a 20 mL standard sample trapped between 0.026-2.6 k *g*.

Size Selection

SnP_3 powder was exfoliated as above and the 28 *g* supernatant was subject to increasing iterative centrifugation steps termed Liquid Cascade centrifugation as described in previous work.[36] The sediment of each centrifugation speed was collected and redispersed in IPA and the supernatant was moved to a higher speed. The speeds used for centrifugation were 0.026, 0.1, 0.4, 1, 1.6 and 2.6 k *g*. Samples were labelled according to the lower and upper centrifugation limits used to produce each fraction. For example, a supernatant was produced after centrifuging at RCF = 400 × g-force (0.4 k *g*) and the resultant supernatant was centrifuged at 1000 g. The sediment collected after the 1 k *g* step was referred to as the 0.4-1k g fraction.

Characterisation

Optical spectra were measured using a Perkin Elmer Lambda 1050 UV-Visible spectrometer with a silica glass cuvette (path length 4 mm). The spectrometer was equipped with an integrating sphere for measuring the absorption where scattering effects are removed. To determine the extinction coefficients, nanosheet concentrations of size selected samples were determined gravimetrically. Samples were filtered through alumina membranes, washed with 500 mL of water and once dried were weighed.

A Horiba Jobin-Yvon LabRAM HR800 was used to acquire the Raman spectra with a 633 nm excitation laser in air under ambient conditions. Laser spot on the sample was focused in 2 μm with 0.2 mW power. Scattered light was collected by a long working distance objective with a magnification of 100×. A diffraction grating of 600 grooves was chosen, obtaining ~1.5 cm^{-1} spectral resolution. Each spectrum is the average of 16 different spectra, each of them integrated for 30 seconds. Measurements were performed on both drop-cast and filtered SnP_3 thin films. Liquid dispersions (15 μL) of size selected samples were diluted until transparent and drop cast onto preheated (180 °C) Si/SiO_2 (300 nm oxide layer) wafers. AFM was subsequently carried out on a Bruker Multimode 8 microscope in ScanAsyst mode with Oltespa R3 cantilevers.

In preparation for TEM imaging, each dispersion was diluted to optical transparency and manually drop-cast one drop at a time onto a holey carbon TEM grid with the aim of dropping approximately 0.1 mg of material. The grids were left to dry in air and then placed overnight in a vacuum oven at 70 °C to dry completely before measuring. Bright field TEM imaging was performed using a JEOL 2100 microscope. Energy-dispersive X-ray (EDX) spectroscopy was performed in situ with TEM imaging using an 80 mm^2 XMAX EDX detector. 36 nanosheets were selected at random and elemental analysis was performed with Cliff Lorimer thin ratio section quantitation method.

SEM images of the SnP_3 powder, the prepared SnP_3 and SnP_3:SWNT composite films were obtained using a Zeiss Ultra Plus scanning electron microscope. Accelerating voltages of 2 - 5 kV, with a 30 μm aperture at a working distance of 3 - 6 mm were used. The pure SnP_3 and the SnP_3:SWNT composite films were imaged on the polymer filtration membrane and the Al current collector, respectively. In order to minimise charging, the sides of the samples were coated with silver paint. Furthermore, the SnP_3:SWNT composite films were snapped at room temperature and the fractured sides were looked at for the cross-sectional images.

Computational details

The structural configuration and Raman spectrum of SnP_3 monolayer and bilayer were calculated using first-principles calculations on the basis of density functional theory (DFT) as implemented in Vienna ab initio simulation package (VASP).[46] We employed a plane wave basis (cutoff energy of 500 eV) together with the projector-augmented plane wave (PAW) approach.[47] The generalized gradient approximation (GGA) using a PBE functional with D3 London dispersion corrections was employed to accurately describe the weak interactions

between SnP_3 layers.[48] A convergence threshold of 10^{-5} eV in energy and 10^{-2} eV $Å^{-1}$ in force within the conjugated gradient method were adopted in all computations. The Monkhorst-Pack k-point mesh of the Brillouin Zone were set to 5 × 5 × 1. The optimized lattice parameter of SnP_3 monolayer is $a = b = 7.16$ Å. A vacuum region of 20 Å in the *c* direction was used to avoid spurious interactions with replicas.

Non-resonant first-order Raman calculations were performed based on the fully relaxed lattice vectors and atomic positions of SnP_3 monolayer. The dynamic matrix and derivatives of the dielectric constant tensor were first calculated based on the density functional perturbation theory (DFPT) as implemented in PHONOPY package. The Raman intensity of the j-th phonon mode was then obtained according to:[49]

$$\frac{d\sigma}{d\Omega} = N_{prim}\frac{\omega_s^4}{c^4 V_{prim}}\left|g_s \bullet \alpha(j) \bullet g_i^T\right|^2 \times \frac{\hbar}{2\omega_j}(n_j + 1)$$

where ω_i and ω_s represent the frequencies of the incoming and scattered light, respectively; ω_j denotes the frequency of the j-th phonon mode. V_{prim} and N_{prim} represent the volume and the number of the primitive unit cell in the sample, and c is the speed of light. n_j is the Bose factor of the j-th phonon mode and is determined by $n_j = (e^{\hbar\omega_j/k_BT} - 1)^{-1}$. g_i and g_s are the polarization vectors of the incoming and scattered light.

Electrochemical Characterisation

The SnP_3 dispersions were mixed in various proportions with dispersions of SWCNTs in IPA. SWCNTs improved both the mechanical stability and electrical conductivity of the resulting films and were the only additives used. Typically, the 0.1 mg mL^{-1} SWCNT dispersions were prepared by adding 8 mg P3-SWCNT to 80 mL IPA and sonicating for 2 hours using a horn-tip sonic probe (Vibracell CVX, 750W) at 60% amplitude with an on/off pulse ratio of 6s/2s.

Electrodes were prepared by vacuum filtration as described below. We acknowledge that it would be better, from a practical standpoint, to prepare electrodes by slurry casting. However, we were unable to prepare good quality nanosheet-based films by slurry casting. We speculate that this is to do with difficulties preparing non-aggregated dispersions at the high concentrations required for slurry casting. We believe further work is required to resolve this question.

For SWCNT dependent study, these mixed dispersions were vacuum-filtered using porous cellulose filter membranes (MF-Millipore membrane mixed cellulose esters, hydrophilic, 0.025 μm, 47 mm). The mass loading of these films was controlled by the volume of dispersion

filtered. The resulting films (diameter, 36 mm) were cut to the desired dimensions for electrochemical testing and then transferred to Cu foil. For transferring, IPA was used to adhere the electrode side of film to the substrate, thus the cellulose filter membrane was exposed to the air. Then, the cellulose filter membrane was removed by treatment with acetone vapor for mins and subsequent acetone liquid baths for 0.5 h. The mass loading of SnP_3 in films was 0.3 mg cm^{-2} for rate capability measurement and cycling performance measurement.

For the thickness-dependent study, the mass loading of these films was controlled by the volume of dispersion filtered. The resulting films (A_{Geo} = 2 cm^2) were cut to the desired dimensions for electrochemical testing. We should notice that the thick films (SnP_3 mass loading > ~1 mg cm^{-2}) were free standing and there was no need to transfer the electrodes onto Cu foil. But to keep consistent, a Cu foil disc (D = 12 mm) was also used as a current collector.

For the half-cell electrochemical characterization, the coin cells were assembled by using Li-metal disc (diameter, 14 mm; MTI Corp.) as the counter/reference electrode in a glovebox filled with highly pure argon gas (O_2 and H_2O levels < 0.1 ppm). Celgard C212 (thickness 16 μm) was used as a separator. Lithium hexafluoridophosphate ($LiPF_6$, 1.2 M) in ethylene carbonate/dimethyl carbonate (EC/DMC, 1:1 in vol/vol, BASF) with 10 wt.% fluoroethylene carbonate (FEC, Sigma Aldrich) was used as the electrolyte for half-cell measurements. Cyclic voltammetry of the cells was carried out using a galvanostat–potentiostat (VMP-3, Biologic) between 0.05 and 3.0 V vs. Li^+/Li at a scanning rate of 0.1 mV s^{-1} for 50 cycles. Impedance measurements were performed using a Biologic VMP-3 with a frequency range of 1 MHz–0.1 Hz and a voltage amplitude of 10 mV. EC-Lab Z-Fit software was used to model the acquired spectra. The electrochemical properties of the SnP_3 anodes were measured within a voltage range of 0.05–3 V by a potentiostat, using the galvanostatic charge/discharge mode (Arbin). The areal capacities (C/A) of the electrodes were obtained by dividing the measured cell capacity by the electrode area (0.178 cm^2). The cyclabilities of the electrodes were evaluated at 1 mA cm^{-2} after initial formation cycle at ~1/20 C rate. The discharge rate capabilities of the electrodes were investigated using symmetric charge/discharge conditions.

For full cells, NCA/CNT and NMC811/CNT electrodes were used as cathodes. Here, we employed $LiNi_{0.815}Co_{0.15}Al_{0.035}O_2$ (NCA, MTI Corporation) powder as an active material. Single-walled nanotubes were purchased from OCSiAl (Tuball, 0.4 wt% CNT in NMP, 2 wt% PVDF as a surfactant stabilizer). Because of the unavoidable polymer stabiliser, the compositions of these electrodes were AM/PVDF/CNT (97:2.5:0.5 by wt.). The AM powers were directly mixed with the CNT solution and ground by a mortar and pestle to obtain a

uniform slurry. Then the slurry was cast onto Al foil using a doctor blade. More details were reported in our previous work.[32]

The full cells were assembled by using our SnP_3/CNT anodes with NCA/CNT or NMC811/CNT cathodes with various C/A (or M/A). We used the same sized cathode/anode disc (0.178 cm^2) to match the C/A of both electrodes. Current collector and separator thicknesses were: Cu foil=10 μm; Al foil=15 μm; separator=16 μm. For SnP_3/CNT-NMC811/CNT full cell, 1.2 M $LiPF_6$ in EC/DMC (1:1 in vol/vol, BASF) with 10 wt% FEC was used as the electrolyte. For SnP_3/CNT-NCA/CNT full cell, 0.6 M Lithium difluorido(oxalato)borate (LiDFOB, Sigma-Aldrich) + 0.6 M Lithium tetrafluoridoborate (LiBF4, Sigma-Aldrich) in fluoroethylene carbonate/diethyl carbonate (FEC/DEC, 1:2 in vol/vol, TCI EUROPE N.V.) was used as electrolyte. The anode and cathode densities were 3.2 and 1.3 g/cm^3 while the anode : cathode (total) mass ratios were kept as close as possible to 1 : 4.5. The N/P ratio, defined by the capacity ratio between the anode and cathode, was balanced to be ~1.1 (see Supplementary Table 4 for details of cathode/anode in full cells). The full cells were then cycled at ~1/7 C rate within a voltage range of 1.5–4.5 V after the initial formation cycle at 1/20 C rate. The total C/A of the full cell was obtained by dividing the measured cell capacity by the geometric electrode area (0.178 cm^2). The charging and discharging rate capabilities of full cells were measured using asymmetric charge/discharge protocols. The discharge rate capabilities were investigated by constant current discharging; the cells were fully charged at ~1/20 C rate, then discharged at varied current densities (CC mode).

DATA AVAILABILITY: All data employed in this work are available from the corresponding author upon reasonable request.

ACKNOWLEDGEMENTS: We acknowledge the European Research Council Advanced Grant (FUTURE-PRINT) and the European Union under grant agreements n°785219 Graphene Flagship-core 2. We have also received support from the Science Foundation Ireland (SFI) funded center AMBER (SFI/12/RC/2278**)** and availed of the facilities of the SFI-funded AML and ARM labs**.** We also thank Nokia-Bell Labs Ireland for continuing support. MMcC thanks the Irish Research Council for funding.

AUTHOR CONTRIBUTIONS: RT, AG, MMcC, MB, AH, CG, DVH, CB, YY, TH, S-HP, JC, VN contributed to acquisition, analysis, **or** interpretation of data. MN, CB and OO supplied materials and contributed to acquisition, analysis, **or** interpretation of data. TH, OO and JNC conceived and designed the work. JNC analysed data and wrote the paper.

COMPETING INTERESTS: The authors declare no competing interests.

Figures

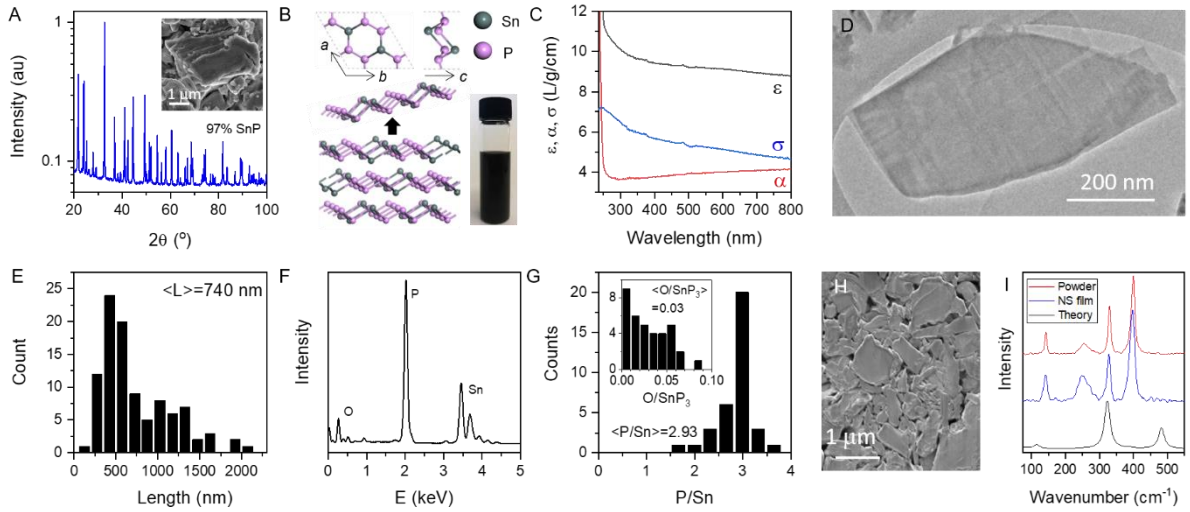

Figure 1: Liquid exfoliation of SnP_3. A) PXRD pattern for SnP_3 bulk material which indicates a composition of 97wt% SnP_3 and 3wt% Sn_3P_4. Inset: SEM image of layered powder. B) Structure of SnP_3 monolayer, schematic illustrating exfoliation and image of SnP_3 nanosheets dispersed in NMP. C) Optical extinction, ε, absorption, α, and scattering, σ, coefficient spectra of an SnP_3 dispersion. D-E) Typical TEM image (D) and nanosheet length histogram (E) of liquid exfoliated SnP_3 nanosheets (standard sample). F) Example of an EDX spectrum measured from a single SnP_3 nanosheet in the TEM. G) Histogram showing nanosheet by nanosheet EDX results for atomic P/Sn ratio and atomic O/SnP_3 ratio (inset). H) SEM image of a thin film of SnP_3 nanosheets. I) Raman spectra measured for Bulk SnP_3 powder as well as a film of liquid exfoliated SnP_3 nanosheets. Also shown is a calculated SnP_3 Raman spectrum.

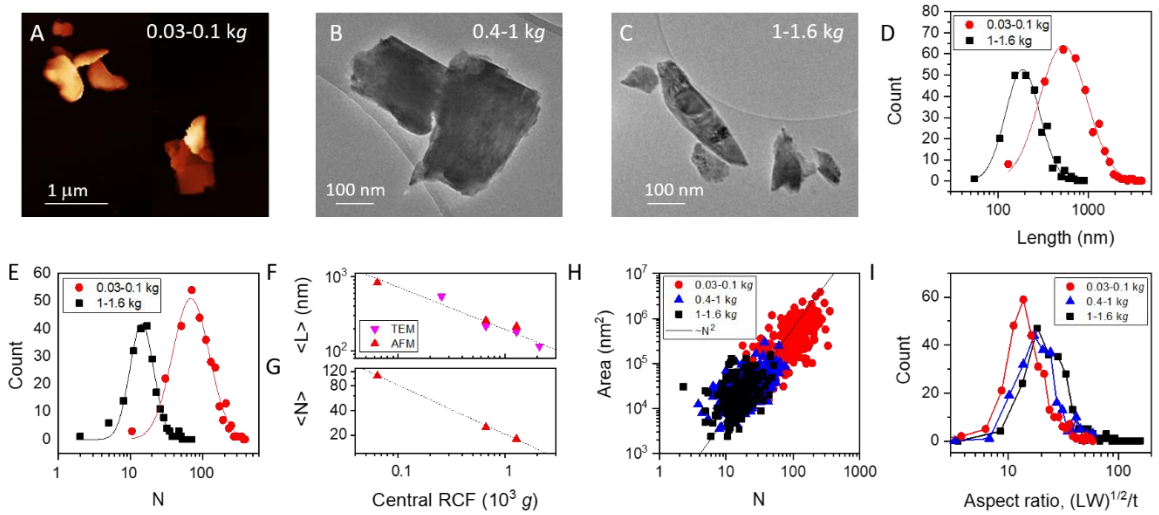

Figure 2: Size selection of liquid exfoliated SnP_3 nanosheets. A) AFM image of nanosheets selected in fraction XL. B-C) Selected TEM images of size-selected nanosheets prepared in fractions M and S. In A-C, the upper and lower centrifugal forces used during size selection are given in the caption. D-E) Nanosheet length (D) and layer-number (i.e. thickness in monolayers, E) histograms measured by AFM for the fractions XL and S. F-G) Nanosheet length (F, from TEM and AFM) and layer number (G, from AFM) plotted versus the central relative centrifugal force used during size selection. The dashed lines represent power-laws with exponents close to -0.5. H) Nanosheet area (approximated as length × width) plotted versus layer number for three different size selected fractions. Data measured by AFM with each point representing an individual nanosheet. The line shows a quadratic (i.e. area $\propto N^2$) fit to the mean values of the data clouds for each fraction. I) Nanosheet aspect ratio (lateral size / thickness, t) histograms for three different size selected fractions (assuming a monolayer thickness of 0.35 nm).[38]

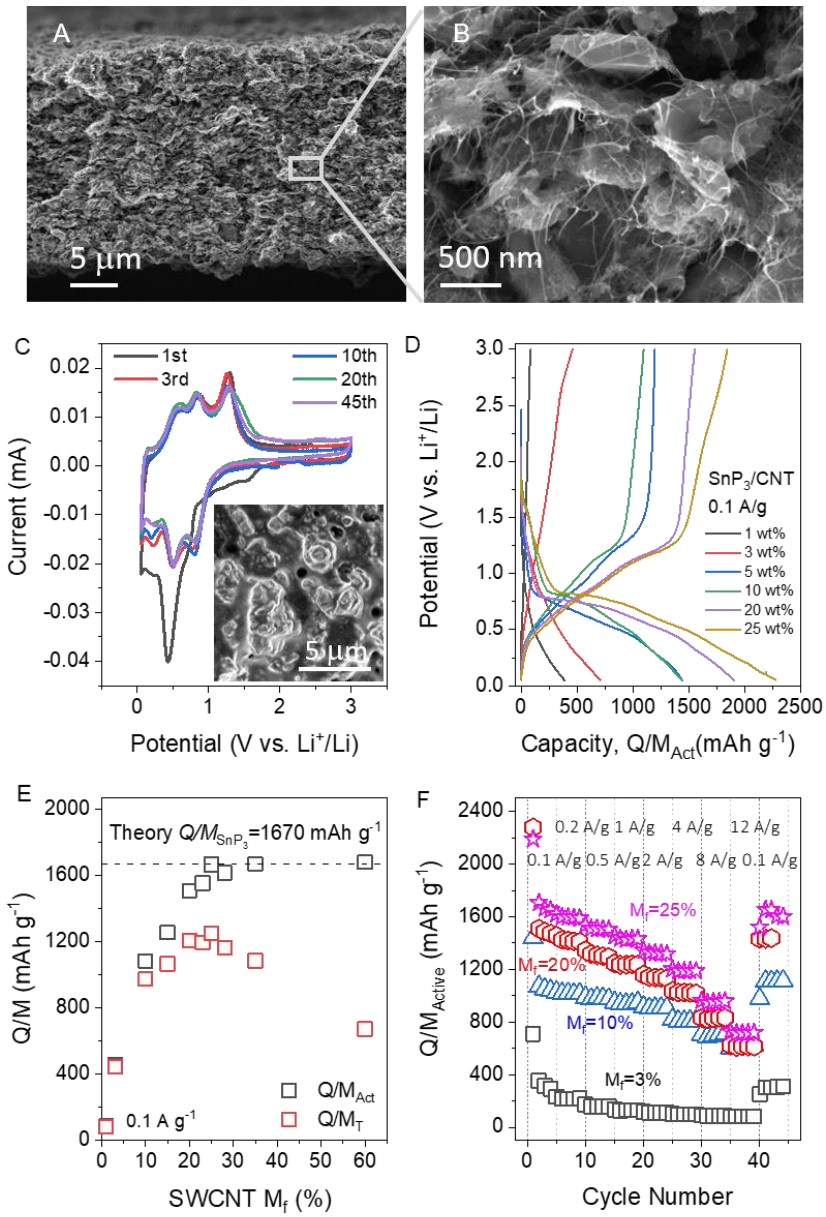

Figure 3: Lithium storage in SnP_3/nanotube composite films. A-B) SEM images at two magnifications of an SnP_3/single walled nanotube composite film (M_f = 25%, M_T/A = 2.3 mg cm^{-2}). C) Cyclic voltammetry of a similar films used as a lithium battery anode (M_f = 25wt%, M_T/A = 0.45 mg cm^{-2}, dV/dt = 0.1 mV s^{-1}). Inset: SEM image of an anode after lithiation. D) Voltage profiles for SnP_3/nanotube composite anodes prepared with various nanotube loadings (I/M_T = 0.1 A g^{-1}, M_T/A = 0.4 mg cm^{-2}). E) Specific charging capacity plotted versus nanotube loading for composite anodes. Data is shown for capacity normalised to both the active mass and the total electrode mass. The dashed line represents the theoretical capacity of SnP_3. F) Cycling stability measured at different currents for composites of three different nanotube loadings.

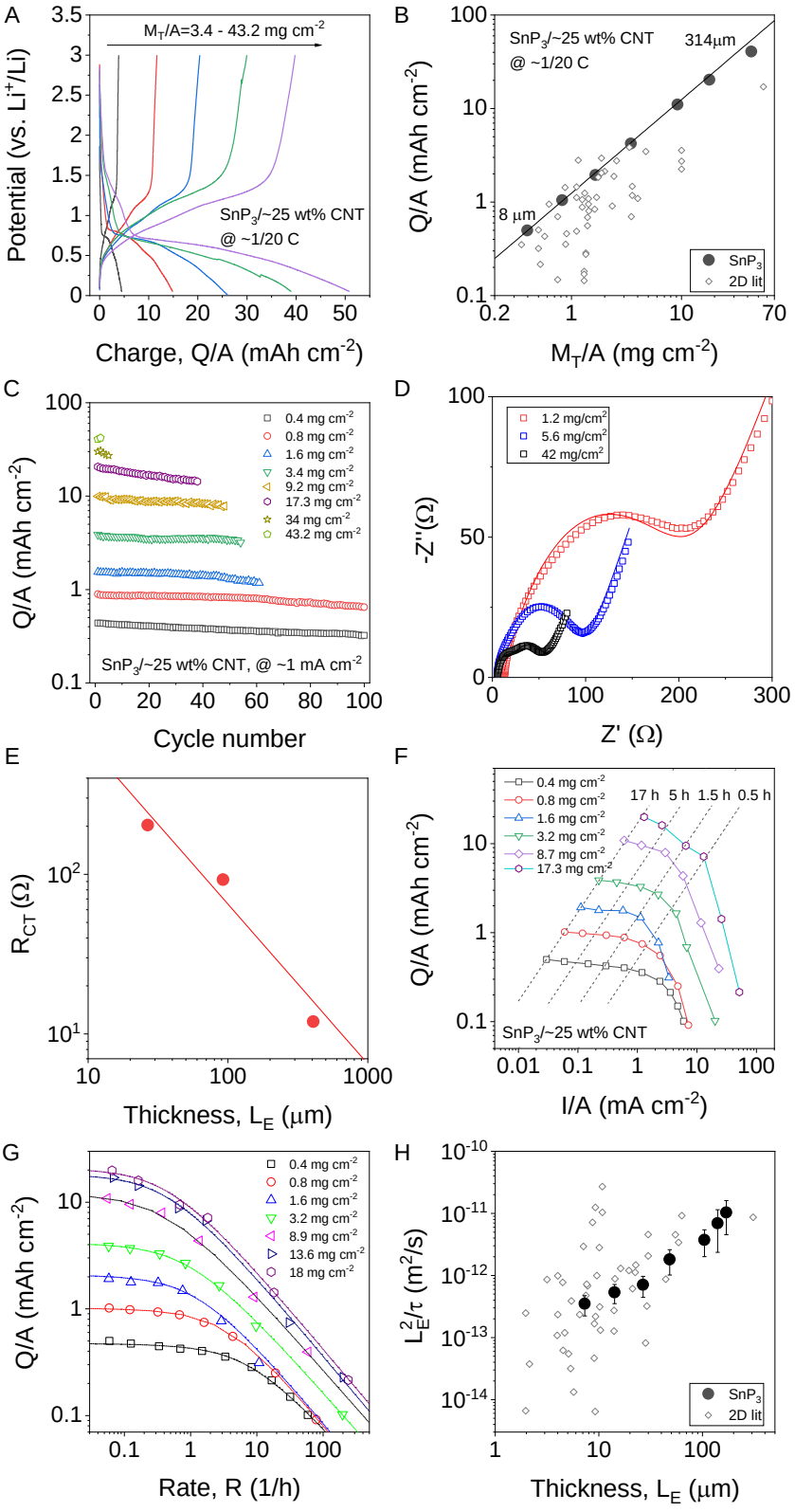

Figure 4: High areal capacity anodes. A) Voltage profiles for SnP_3/nanotube composite anodes prepared with various mass loadings i.e. electrode thicknesses (C-rate ≈ 1/20 C, M_f = 25%). B)

Areal capacity plotted as a function of total electrode mass loading, M_T/A. The solid line represents a specific capacity of Q/M_T = 1250 mAh g^{-1} (C-rate ≈ 1/20C, M_f = 25%). The thicknesses of the thickest and thinnest electrodes are indicated in the panel. Grey data points represent literature values for 2D-based electrodes extracted from ref[12]. C) Areal charging capacity as a function of cycle number for SnP_3/nanotube composite anodes of various mass loadings (I/A ≈ 1 mA cm^{-2}, M_f = 25%, see details of Coulombic Efficiency (CE) vs. cycle number in Supplementary Figure 9). D) Impedance spectra for SnP_3/nanotube composite anodes of three mass loadings including fits (see Supplementary Table 3 for all fit parameters). E) charge transfer resistance plotted versus electrode thickness. The line indicates inverse dependence. F) Areal capacity as a function of discharge current density for SnP_3/nanotube composite anodes of various mass loadings (M_T/A). The dashed lines are contours of constant discharge time. G). Areal capacity plotted versus rate, R, for SnP_3/CNT anodes of various mass loadings. The lines are fits to equation 2. Here rate is defined as R = (I/A)/(Q/A). H) Plot of the square of electrode thickness divided by the characteristic time associated with charge/discharge, L_E^2/τ, plotted *versus* electrode thickness, L_E. Here, better rate performance is associated with high values of L_E^2/τ. For comparison literature data for 2D material-based batteries extracted from ref [12] is also shown.

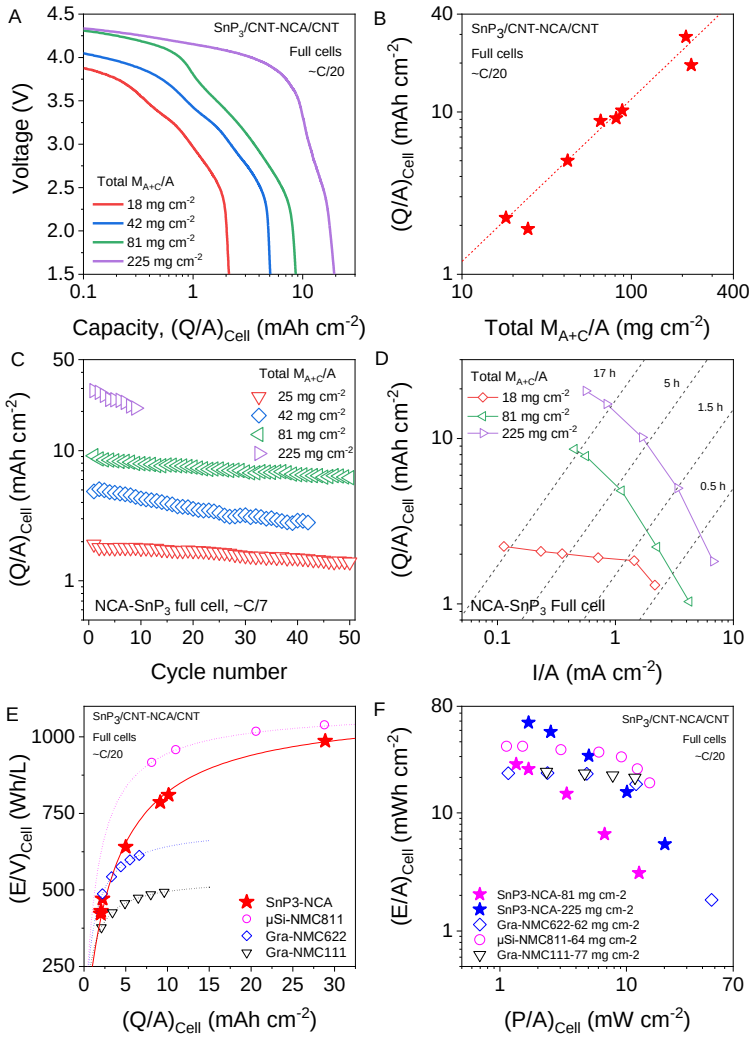

Figure 5: Characterisation of full cells based on SnP_3/CNT anodes and NCA/CNT cathodes. A) Voltage profiles of full cells with SnP_3/nanotube composite anodes combined with NCA/CNT composite cathodes. Each cell has different electrode loading expressed as the combined anode and cathode total loading (C-rate ≈ C/20, anode M_f = 25wt%, cathode M_f = 0.5wt%). B) Full cell areal capacity plotted as a function of total anode plus cathode mass loading, M_{A+C}/A (C-rate ≈ C/20). C) Cell areal capacity as a function of cycle number for the full cells shown in A (C-rate ≈ C/7, see details of Coulombic Efficiency (CE) vs. cycle number in Supplementary Figure 14). D) Cell areal capacity as a function of discharge current density for full cells of two different mass loadings. E) Plot of cell volumetric energy density, versus cell areal capacity (both measured at C/20) for SnP_3/CNT - NCA/CNT full cells of various thicknesses (see Supplementary Table 4 for details). For comparison, we plot equivalent data for state-of-the-art full cells based on Si-NMC,[18] and graphite-NMC (see Supplementary Table 5 for details).[44] The lines are fits to equation 6. F) Ragone plot of cell energy versus

power, both normalised to cell area for SnP_3/CNT - NCA/CNT full cells of two different thicknesses, measured at various currents. Shown for comparison are data for the literature cells shown in E.

References

[1] Z. P. Cano, D. Banham, S. Y. Ye, A. Hintennach, J. Lu, M. Fowler, Z. W. Chen, Nat. Energy 2018, 3, 279.
[2] G. Zubi, R. Dufo-Lopez, M. Carvalho, G. Pasaoglu, Renew. Sust. Energ. Rev. 2018, 89, 292.
[3] H. Zhang, H. Zhao, M. A. Khan, W. Zou, J. Xu, L. Zhang, J. Zhang, J. Mater. Chem. C. 2018, 6, 20564.
[4] S.-H. Park, R. Tian, J. Coelho, V. Nicolosi, J. N. Coleman, Adv. Energy Mater. 2019, 9, 1901359.
[5] K. Kubota, M. Dahbi, T. Hosaka, S. Kumakura, S. Komaba, Chem. Rec. 2018, 18, 459.
[6] X. B. Zang, T. Wang, Z. Y. Han, L. T. Li, X. Wu, NANO 2019, 14, 14.
[7] F. Bonaccorso, L. Colombo, G. H. Yu, M. Stoller, V. Tozzini, A. C. Ferrari, R. S. Ruoff, V. Pellegrini, Science 2015, 347, 1246501.
[8] C. L. Tan, X. H. Cao, X. J. Wu, Q. Y. He, J. Yang, X. Zhang, J. Z. Chen, W. Zhao, S. K. Han, G. H. Nam, M. Sindoro, H. Zhang, Chem. Rev. (Washington, DC, U. S.) 2017, 117, 6225.
[9] J. N. Coleman, M. Lotya, A. O'Neill, S. D. Bergin, P. J. King, U. Khan, K. Young, A. Gaucher, S. De, R. J. Smith, I. V. Shvets, S. K. Arora, G. Stanton, H. Y. Kim, K. Lee, G. T. Kim, G. S. Duesberg, T. Hallam, J. J. Boland, J. J. Wang, J. F. Donegan, J. C. Grunlan, G. Moriarty, A. Shmeliov, R. J. Nicholls, J. M. Perkins, E. M. Grieveson, K. Theuwissen, D. W. McComb, P. D. Nellist, V. Nicolosi, Science 2011, 331, 568.
[10] V. Nicolosi, M. Chhowalla, M. G. Kanatzidis, M. S. Strano, J. N. Coleman, Science 2013, 340, 1420.
[11] K. Chang, W. X. Chen, Chem. Commun. 2011, 47, 4252.
[12] R. Tian, M. Breshears, D. V. Horvath, J. N. Coleman, ACS Nano 2020, 14, 3129.
[13] P. Xiong, L. L. Peng, D. H. Chen, Y. Zhao, X. Wang, G. H. Yu, Nano Energy 2015, 12, 816.
[14] H. Y. Sun, A. E. D. Castillo, S. Monaco, A. Capasso, A. Ansaldo, M. Prato, D. A. Dinh, V. Pellegrini, B. Scrosati, L. Manna, F. Bonaccorso, J. Mater. Chem. C. 2016, 4, 6886.
[15] R. H. Wang, C. H. Xu, J. Sun, Y. Q. Liu, L. Gao, H. L. Yao, C. C. Lin, Nano Energy 2014, 8, 183.
[16] J. Sun, H.-W. Lee, M. Pasta, H. Yuan, G. Zheng, Y. Sun, Y. Li, Y. Cui, Nat. Nanotechnol. 2015, 10, 980.
[17] Y. L. Cao, M. Li, J. Lu, J. Liu, K. Amine, Nat. Nanotechnol. 2019, 14, 200.
[18] S.-H. Park, P. J. King, R. Tian, C. S. Boland, J. Coelho, C. Zhang, P. McBean, N. McEvoy, M. P. Kremer, D. Daly, J. N. Coleman, V. Nicolosi, Nat. Energy 2019, 4, 560.
[19] S. J. Kim, M. Naguib, M. Q. Zhao, C. F. Zhang, H. T. Jung, M. W. Barsoum, Y. Gogotsi, Electrochim. Acta 2015, 163, 246.
[20] N. Nitta, F. X. Wu, J. T. Lee, G. Yushin, Mater. Today 2015, 18, 252.
[21] F. Hulliger, *Structural Chemistry of Layer-Type Phases*, Springer, Netherlands 1976; S. Haastrup, M. Strange, M. Pandey, T. Deilmann, P. S. Schmidt, N. F. Hinsche, M. N. Gjerding, D. Torelli, P. M. Larsen, A. C. Riis-Jensen, J. Gath, K. W. Jacobsen, J. Jørgen Mortensen, T. Olsen, K. S. Thygesen, 2D Mater. 2018, 5, 042002.
[22] N. Mounet, M. Gibertini, P. Schwaller, D. Campi, A. Merkys, A. Marrazzo, T. Sohier, I. E. Castelli, A. Cepellotti, G. Pizzi, N. Marzari, Nat. Nanotechnol. 2018, 13, 246.
[23] Y. Jing, Y. Ma, Y. Li, T. Heine, Nano Lett. 2017, 17, 1833.
[24] S. Sun, F. Meng, H. Wang, H. Wang, Y. Ni, J. Mater. Chem. C. 2018, 6, 11890.
[25] J. W. Park, C. M. Park, Sci. Rep. 2016, 6.

[26] X. L. Fan, J. F. Mao, Y. J. Zhu, C. Luo, L. M. Suo, T. Gao, F. D. Han, S. C. Liou, C. S. Wang, Adv. Energy Mater. 2015, 5.
[27] G. Du, Z. Guo, S. Wang, R. Zeng, Z. Chen, H. Liu, Chem. Commun. 2010, 46, 1106; Y. D. Liu, L. Ren, X. Qi, L. W. Yang, J. Li, Y. Wang, J. X. Zhong, Journal of Energy Chemistry 2014, 23, 207.
[28] J. B. Boland, A. Harvey, R. Tian, V. Vega-Mayoral, A. Griffin, C. Gabbett, M. Breshears, J. Pepper, Y. Li, J. N. Coleman, 2D Mater. 2019, 7, 035015.
[29] Y. P. Liu, X. Y. He, D. Hanlon, A. Harvey, U. Khan, Y. G. Li, J. N. Coleman, ACS Nano 2016, 10, 5980.
[30] V. Vega-Mayoral, R. Y. Tian, A. G. Kelly, A. Griffin, A. Harvey, M. Borrelli, K. Nisi, C. Backes, J. N. Coleman, Nanoscale 2019, 11, 6206.
[31] C. Gabbett, C. S. Boland, A. Harvey, V. Vega-Mayoral, R. J. Young, J. N. Coleman, Chem. Mater. 2018, 30, 5245.
[32] R. Tian, N. Alcala, S. J. K. O'Neill, D. V. Horvath, J. Coelho, A. J. Griffin, Y. Zhang, V. Nicolosi, C. O'Dwyer, J. N. Coleman, ACS Applied Energy Materials 2020, 3, 2966.
[33] R. Tian, S.-N. Park, P. J. King, G. Cunningham, J. Coelho, V. Nicolosi, J. N. Coleman, Nature Commun. 2019, 10, 1933.
[34] F. Bonaccorso, A. Bartolotta, J. N. Coleman, C. Backes, Adv. Mater. 2016, 28, 6136.
[35] C. Backes, D. Campi, B. M. Szydlowska, K. Synnatschke, E. Ojala, F. Rashvand, A. Harvey, A. Griffin, Z. Sofer, N. Marzari, J. N. Coleman, D. D. O'Regan, ACS Nano 2019, 13, 7050.
[36] C. Backes, B. M. Szydlowska, A. Harvey, S. J. Yuan, V. Vega-Mayoral, B. R. Davies, P. L. Zhao, D. Hanlon, E. J. G. Santos, M. I. Katsnelson, W. J. Blau, C. Gadermaier, J. N. Coleman, ACS Nano 2016, 10, 1589.
[37] A. Harvey, C. Backes, J. B. Boland, X. Y. He, A. Griffin, B. Szydlowska, C. Gabbett, J. F. Donegan, J. N. Coleman, Nature Commun. 2018, 9, 4553.
[38] P. L. Gong, F. Zhang, L. F. Huang, H. Zhang, L. Li, R. C. Xiao, B. Deng, H. Pan, X. Q. Shi, J Phys Condens Matter 2018, 30, 475702.
[39] C. F. Zhang, S. H. Park, O. Ronan, A. Harvey, A. Seral-Ascaso, Z. F. Lin, N. McEvoy, C. S. Boland, N. C. Berner, G. S. Duesberg, P. Rozier, J. N. Coleman, V. Nicolosi, Small 2017, 13, 1701677; B. Zhang, Y. Yu, Y. Liu, Z.-D. Huang, Y.-B. He, J.-K. Kim, Nanoscale 2013, 5.
[40] H. L. Ye, L. Wang, S. Deng, X. Q. Zeng, K. Q. Nie, P. N. Duchesne, B. Wang, S. Liu, J. H. Zhou, F. P. Zhao, N. Han, P. Zhang, J. Zhong, X. H. Sun, Y. Y. Li, Y. G. Li, J. Lu, Adv. Energy Mater. 2017, 7.
[41] D. V. Horváth, J. Coelho, R. Tian, V. Nicolosi, J. N. Coleman, ACS Applied Energy Materials 2020, 3, 10154.
[42] M. Zhou, X. Li, B. Wang, Y. Zhang, J. Ning, Z. Xiao, X. Zhang, Y. Chang, L. Zhi, Nano Lett. 2015, 15, 6222.
[43] J. N. Coleman, R. Tian, Current Opinion in Electrochemistry 2020, 21, 1.
[44] K. G. Gallagher, S. E. Trask, C. Bauer, T. Woehrle, S. F. Lux, M. Tschech, P. Lamp, B. J. Polzin, S. Ha, B. Long, Q. L. Wu, W. Q. Lu, D. W. Dees, A. N. Jansen, J. Electrochem. Soc. 2016, 163, A138; M. Singh, J. Kaiser, H. Hahn, J. Electrochem. Soc. 2015, 162, A1196; M. Singh, J. Kaiser, H. Hahn, J. Electroanal. Chem. 2016, 782, 245.
[45] A. E. Del Rio Castillo, V. Pellegrini, A. Ansaldo, F. Ricciardella, H. Sun, L. Marasco, J. Buha, Z. Dang, L. Gagliani, E. Lago, N. Curreli, S. Gentiluomo, F. Palazon, M. Prato, R. Oropesa-Nuñez, P. S. Toth, E. Mantero, M. Crugliano, A. Gamucci, A. Tomadin, M. Polini, F. Bonaccorso, Materials Horizons 2018, 5, 890.
[46] G. Kresse, J. Hafner, Phys. Rev. B 1993, 47, 558.
[47] P. E. Blochl, Phys. Rev. B 1994, 50, 17953.
[48] S. Grimme, J. Comput. Chem. 2006, 27, 1787; J. P. Perdew, K. Burke, M. Ernzerhof, Phys. Rev. Lett. 1996, 77, 3865.
[49] M. Ceriotti, F. Pietrucci, M. Bernasconi, Phys. Rev. B 2006, 73, 104304; P. Umari, A. Pasquarello, A. Dal Corso, Phys. Rev. B 2001, 63, 094305.